1

Comparison of Time Implicit Symmetric Gauss-Seidel Iterative Schemes for Computation of Hypersonic Nonequilibrium Flow

Chang Ho Lee* and Seung O Park**

Department of Aerospace Engineering
KAIST, Taejon City, Korea 305-701

Abstract

The time implicit point SGS scheme is applied to compute hypersonic viscous flows in thermochemical nonequilibrium. The performance of the point SGS scheme is then compared with those of the line SGS and the LU-SGS schemes. Comparison of convergence histories with the effect of multiple forward and backward sweeps are made for the flow over a 2D cylinder experimentally studied by Hornung and the flow over a hemisphere at conditions corresponding to the peak heating condition during the reentry flight of an SSTO vehicle. Results indicate that the point SGS scheme with multiple sweeps is as robust and efficient as the line SGS scheme. For the point SGS and the LU-SGS scheme, the rate of improvement in convergence is largest with two sweep cycles. However, for the line SGS scheme, it is found that more than one sweep cycle deteriorates the convergence rate.

Key Word : thermochemical nonequilibrium, Navier-Stokes equations, symmetric Gauss-Seidel, multiple sweeps

Introduction

The flowfield around a hypersonic vehicle is characterized by a strong bow shock, steep gradients of velocity and temperature in the boundary layer, and thermochemical nonequilibrium processes due to high temperature. In the process of time integration of governing equations for such flows, stiffness problem often arise owing to chemical reactions. Stiffness can be interpreted as a disparity between the characteristic time scales of chemical source terms and the characteristic time scales of convective and diffusion terms.

Many researchers have made efforts to develop robust and efficient implicit schemes to overcome the stiffness problem of chemically reacting flows [1-5]. Relaxation schemes based on Gauss-Seidel method turned out to be robust and efficient, since strong diagonally dominant solution matrices could be achieved with upwind schemes. The line symmetric Gauss-Seidel (line SGS) scheme of Candler and MacCormack [1] is known as one of the most efficient implicit schemes, and has been widely used for chemically reacting flows as well as perfect gas flows. The lower-upper symmetric Gauss-Seidel (LU-SGS) scheme with the diagonal approximation of chemical source Jacobian by Eberhardt and Imlay [3] accomplishes much less CPU load per iteration and reduction in memory because it requires only scalar diagonal matrix

---

* Graduate student
** Professor
E-mail: sopark@kaist.ac.kr, TEL : 042-869-3713, FAX : 042-869-3710

inversion. However, this scheme has some problems associated with the diagonal approximation of chemical source Jacobian. Hassan et al. [4] pointed out that the diagonal approximation of Eberhardt and Imlay was not appropriate to represent the chemical time scale of each species, and proposed an alternative method while it requires the changes of equations set to include elemental densities. The point symmetric Gauss–Seidel (point SGS) scheme has demonstrated several desirable features for perfect gas flows. It has been found to be more efficient than the line SGS scheme for incompressible flows [6], and easy to extend to three dimensions without factorization error for compressible flows [7]. Further, the point SGS scheme can be vectorized in any dimension and is a good candidate for massively parallel computing [6].

In this work, we examine the performance of the point SGS scheme in comparison with the line SGS and the LU–SGS scheme for hypersonic viscous flows with nonequilibrium chemistry and vibrational excitation. The three implicit schemes for time integration are incorporated into the present code to yield computational results for adequate comparison. Numerical simulations are performed for hypersonic flows over blunt bodies at relatively low and high Mach numbers. Results of convergence history are compared for the three implicit schemes with the effect of multiple sweep cycles.

Governing Equations and Physical Models

The set of governing equations for the present nonequilibrium flow is composed of species mass conservation, momentum conservation, total energy conservation, and vibrational energy conservation. The extended Navier–Stokes equations for two dimensional or axisymmetric flows can be written as

$$\frac{\partial Q}{\partial t} + \frac{\partial (F - F_v)}{\partial x} + \frac{\partial (G - G_v)}{\partial y} + \alpha (H - H_v) = W \tag{1}$$

where $\alpha = 0$ for two dimensional and $\alpha = 1$ for axisymmetric flows. The components of conserved variables vector Q, inviscid flux vectors F and G, viscous flux vectors F_v and G_v, source vectors for axisymmetric geometry H and H_v, and source vector for thermochemistry W are given as follows:
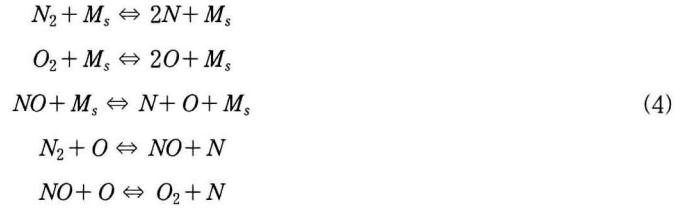
$$
Q = \begin{bmatrix} \rho_1 \\ \rho_2 \\ \vdots \\ \rho_{ns} \\ \rho u \\ \rho v \\ \rho E \\ \rho E_v \end{bmatrix}
\quad
F = \begin{bmatrix} \rho_1 u \\ \rho_2 u \\ \vdots \\ \rho_{ns} u \\ \rho u^2 + p \\ \rho u v \\ (\rho E + p)u \\ \rho E_v u \end{bmatrix}
\quad
G = \begin{bmatrix} \rho_1 v \\ \rho_2 v \\ \vdots \\ \rho_{ns} v \\ \rho u v \\ \rho v^2 + p \\ (\rho E + p)v \\ \rho E_v v \end{bmatrix}
\quad
F_v = \begin{bmatrix} -J_{1x} \\ -J_{2x} \\ \vdots \\ -J_{ns\,x} \\ \tau_{xx} \\ \tau_{xy} \\ u\tau_{xx} + v\tau_{xy} - q_x \\ -q_{vx} \end{bmatrix}
\quad
G_v = \begin{bmatrix} -J_{1y} \\ -J_{2y} \\ \vdots \\ -J_{ns\,y} \\ \tau_{xy} \\ \tau_{yy} \\ u\tau_{xy} + v\tau_{yy} - q_y \\ -q_{vy} \end{bmatrix}
\quad
W = \begin{bmatrix} w_1 \\ w_2 \\ \vdots \\ w_{ns} \\ 0 \\ 0 \\ 0 \\ w_v \end{bmatrix}
$$

$$
H = \frac{1}{y}\begin{bmatrix} \rho_1 v \\ \rho_2 v \\ \vdots \\ \rho_{ns} v \\ \rho u v \\ (\rho E + p)v \\ \rho E_v v \end{bmatrix}
\quad
H_v = \frac{1}{y}\begin{bmatrix} -J_{1y} \\ -J_{2y} \\ \vdots \\ -J_{ns\,y} \\ \tau_{xy} - \dfrac{2}{3}y\dfrac{\partial}{\partial x}\left(\dfrac{\mu v}{y}\right) \\ \tau_{yy} - \tau_{\theta\theta} - \dfrac{2}{3}\dfrac{\mu v}{y} - \dfrac{2}{3}\dfrac{\partial}{\partial y}\left(\dfrac{\mu v}{y}\right) \\ u\tau_{xy} + v\tau_{yy} - q_y - \dfrac{2}{3}\dfrac{\mu v^2}{y} - \dfrac{2}{3}y\dfrac{\partial}{\partial y}\left(\dfrac{\mu v^2}{y}\right) - \dfrac{2}{3}y\dfrac{\partial}{\partial x}\left(\dfrac{\mu u v}{y}\right) \\ -q_{vy} \end{bmatrix}
\tag{2}
$$

where ρ_s is the density of species s, ρ is the mixture density, $\rho = \sum_{s=1}^{ns} \rho_s$, u and v are the velocity components in the x and y directions, respectively, p is the pressure, E is the total energy per unit mass, E_v is the vibrational energy per unit mass, w_s is the mass production rate of species s, and w_v is the production rate of vibrational energy. The diffusion mass flux for species s, J_{sx}, is given by Fick's law with a single diffusion coefficient. The heat fluxes are composed of conduction and diffusion components as

$$q_x = -(k_t + k_r)\frac{\partial T}{\partial x} - k_v \frac{\partial T_v}{\partial x} - \rho \sum_{s=1}^{ns} D \frac{\partial c_s}{\partial x} h_s \tag{3}$$

The viscosity and thermal conductivity (translational, rotational, and vibrational) are determined from the procedures of Reference 1. The mass diffusion coefficient is taken to be the same for all species and calculated assuming a constant Schmidt number of 0.5. The translational and rotational energy modes are assumed to be in equilibrium and described by the translational temperature T. The vibrational energy is determined by assuming a harmonic oscillator and characterized by a single vibrational temperature T_v. A simple non-ionized reacting air model with five species (N_2, O_2, NO, N, O) is considered. For this model, there are three dissociation reactions for the molecules and two exchange reactions involving NO as follows:

$$N_2 + M_s \Leftrightarrow 2N + M_s$$
$$O_2 + M_s \Leftrightarrow 2O + M_s$$
$$NO + M_s \Leftrightarrow N + O + M_s \tag{4}$$
$$N_2 + O \Leftrightarrow NO + N$$
$$NO + O \Leftrightarrow O_2 + N$$

For the reaction rate coefficients, the two-temperature model of Park [8] is employed. In the modeling of vibrational relaxation, the vibration-translation energy exchanges described by the Landau-Teller model and the vibration-dissociation energy exchanges are taken into account as

$$w_v = \sum_{s=1}^{nd} \rho_s \frac{e_{vs}^{eq} - e_{vv}}{\tau_{vs}} + \sum_{s=1}^{nd} w_s e_{vs} \tag{5}$$

where the terms e_{vs}^{eq} and e_{vs} are the vibrational energy of species at the translational and vibrational temperatures, respectively. The vibrational relaxation time of species, τ_{vs}, is determined from the corrected Millikan and White formula by Park [9].

At the body surface, no-slip condition for velocity, constant temperature($T = T_v = T_w$), and zero normal pressure gradient ($\partial p / \partial n = 0$) are imposed.

Numerical Methods

Equation (1) is transformed into a generalized coordinate system, (ξ, η), where ξ is the direction along the body surface, η is the direction normal to the body surface. Using the finite volume method, we obtain a semi-discrete conservation approximation of Eq. (1) with unit spacing, $\Delta \xi = \Delta \eta = 1$, as follows:

$$\left(\frac{1}{J}\frac{\partial \boldsymbol{Q}}{\partial t}\right)_{i,j} + (\widetilde{\boldsymbol{F}} - \widetilde{\boldsymbol{F}_v})_{i+1/2,j} + (\widetilde{\boldsymbol{F}} - \widetilde{\boldsymbol{F}_v})_{i-1/2,j} + (\widetilde{\boldsymbol{G}} - \widetilde{\boldsymbol{G}_v})_{i,j+1/2} + (\widetilde{\boldsymbol{G}} - \widetilde{\boldsymbol{G}_v})_{i,j-1/2}$$
$$+ \alpha \frac{1}{J}(\boldsymbol{H} - \boldsymbol{H}_v)_{i,j} - \frac{1}{J}\boldsymbol{W}_{i,j} = 0 \tag{6}$$

The dependent variables are defined at the cell center (i,j), and the metric terms are defined at the cell interfaces. A tilde denotes numerically approximated flux at the cell interface. Equation (6) provides a set of coupled ordinary differential equations with respect to time. Application of the implicit Euler backward scheme and the time linearization of the nonlinear terms result in

$$\left[\frac{\boldsymbol{I}}{J\varDelta t} + \left(\frac{\partial \boldsymbol{R}}{\partial \boldsymbol{Q}}\right)^n\right]\varDelta \boldsymbol{Q}^n = -\boldsymbol{R}^n(\boldsymbol{Q}) \tag{7}$$

where $\varDelta \boldsymbol{Q}^n = \boldsymbol{Q}^{n+1} - \boldsymbol{Q}^n$. The residual vector $\boldsymbol{R}(\boldsymbol{Q})$ is given as

$$\boldsymbol{R}(\boldsymbol{Q}) = (\widetilde{\boldsymbol{F}} - \widetilde{\boldsymbol{F}_v})_{i+1/2,j} + (\widetilde{\boldsymbol{F}} - \widetilde{\boldsymbol{F}_v})_{i-1/2,j} + (\widetilde{\boldsymbol{G}} - \widetilde{\boldsymbol{G}_v})_{i,j+1/2} + (\widetilde{\boldsymbol{G}} - \widetilde{\boldsymbol{G}_v})_{i,j-1/2}$$
$$+ \alpha \frac{1}{J}(\boldsymbol{H} - \boldsymbol{H}_v)_{i,j} - \frac{1}{J}\boldsymbol{W}_{i,j} \tag{8}$$

For the evaluation of inviscid numerical fluxes, $\widetilde{\boldsymbol{F}}$, $\widetilde{\boldsymbol{G}}$, in the explicit part (right-hand side), we adopt the modified low-diffusion flux-splitting scheme [10] which ensures monotone shock capturing and accuracy in the viscous shear layers. The inviscid numerical flux in the ξ direction is given by

$$\widetilde{\boldsymbol{F}}_{i+1/2,j} = \frac{|\nabla \xi|}{J}(C^+ a_L \boldsymbol{\Phi}_L + C^- a_R \boldsymbol{\Phi}_R) + \frac{|\nabla \xi|}{J}\boldsymbol{\Psi}(D^+ p_L + D^- p_R) \tag{9}$$

where,

$$\boldsymbol{\Phi} = (\rho_1, \rho_2, \cdots, \rho_{ns}, \rho u, \rho v, \rho h_t, \rho E_v)^T \quad , \quad \boldsymbol{\Psi} = (0,0,\cdots,0,\hat{\xi}_x,\hat{\xi}_y,0,0)^T \tag{10}$$

In Eq. (9), subscripts L and R represent the left and right state of the cell interface respectively, a the frozen speed of sound, C^+ the split Mach numbers, and $D^\pm$ the split pressures. Detailed descriptions of the split Mach numbers and the split pressures can be found in Reference 9. To get higher-order accuracy in space, we employ the MUSCL approach [11] which uses the interpolation of primitive variables, , for the construction of the left and right state of conserved variables. The Van Albada limiter function is used to eliminate oscillations in the shock region.

In the implicit part (left-hand side), the firsr-order Van Leer flux vector splitting (FVS) scheme is used for the inviscid flux because it is simple for the construction of flux Jacobian and because the modified LDFSS adopted in discretizing the explicit part is based on FVS. For example, the Jacobian of inviscid flux in the ξ direction at point (i,j) is calculated as

$$\widehat{\boldsymbol{A}}^+(\boldsymbol{Q}_j, \Gamma_{i+1/2}) = \frac{\partial \widetilde{\boldsymbol{F}}_{i+1/2,j}}{\partial \boldsymbol{Q}_i} = \frac{|\varDelta \xi|}{J}\left(C_{VL}^+ a_i \frac{\partial \boldsymbol{\Phi}_i}{\partial \boldsymbol{Q}_i} + a_i \boldsymbol{\Phi}_i \frac{\partial C_{VL}^+}{\partial M_i}\frac{\partial M_i}{\partial \boldsymbol{Q}_i}\right)$$
$$+ \frac{|\varDelta \xi|}{J}\boldsymbol{\Psi}\left(D^+\frac{\partial p_i}{\partial \boldsymbol{Q}_i} + p_i \frac{\partial D^+}{\partial M_i}\frac{\partial M_i}{\partial \boldsymbol{Q}_i}\right) \tag{11}$$

where the symbol $\Gamma_{i+1/2,j}$ represents the metric terms at the cell interface where the numerical flux is to be evaluated and C_{VL}^+ the split Mach number of Van Leer. We retain only viscous flux terms of non-mixed derivative. Thus, the residual vector in the implicit part is dependent on the states of five grid point stencil. The Jacobian of thermochemistry source vector is evaluated as follows.

$$Z = \frac{\partial W}{\partial Q} = \frac{\partial W}{\partial Q}\bigg)_{T, T_v} + \frac{\partial W}{\partial T}\bigg)_{T_v} \frac{\partial T}{\partial Q} + \frac{\partial W}{\partial T_v}\bigg)_{T} \frac{\partial T_v}{\partial Q} \quad (12)$$

The resulting matrix equation with the Jacobians of inviscid fluxes, viscous fluxes, and thermochemistry source term can be written at a point (i, j) as

$$C_1 \Delta Q_{i,j}^n + C_2 \Delta Q_{i-1,j}^n + C_3 \Delta Q_{i,j-1}^n + C_4 \Delta Q_{i+1,j}^n + C_5 \Delta Q_{i,j+1}^n = -R_{i,j}^n \quad (13)$$

where each of coefficients is a 9×9 matrix and has the following form:

$$
\begin{aligned}
C_1 = & \frac{I}{J \Delta t} + \widehat{A}^+(Q_{i,j}, \Gamma_{i+1/2,j}) - \widehat{A}^-(Q_{i,j}, \Gamma_{i-1/2,j}) + \widehat{B}^+(Q_{i,j}, \Gamma_{i,j+1/2}) - \widehat{B}^-(Q_{i,j}, \Gamma_{i,j-1/2}) \\
& + \widehat{A}_v(Q_{i,j}, \Gamma_{i+1/2,j}) + \widehat{A}_v(Q_{i,j}, \Gamma_{i-1/2,j}) + \widehat{B}_v(Q_{i,j}, \Gamma_{i,j+1/2}) + \widehat{B}_v(Q_{i,j}, \Gamma_{i,j-1/2}) + \frac{1}{J} Z_{i,j} \\[4pt]
C_2 = & -\widehat{A}^+(Q_{i-1,j}, \Gamma_{i-1/2,j}) - \widehat{A}_v(Q_{i-1,j}, \Gamma_{i-1/2,j}) \\[4pt]
C_3 = & -\widehat{B}^+(Q_{i,j-1}, \Gamma_{i,j-1/2}) - \widehat{B}_v(Q_{i,j-1}, \Gamma_{i,j-1/2}) \\[4pt]
C_4 = & \widehat{A}^-(Q_{i+1,j}, \Gamma_{i+1/2,j}) - \widehat{A}_v(Q_{i+1,j}, \Gamma_{i+1/2,j}) \\[4pt]
C_5 = & \widehat{B}^-(Q_{i,j+1}, \Gamma_{i,j+1/2}) - \widehat{B}_v(Q_{i,j+1}, \Gamma_{i,j+1/2})
\end{aligned}
\quad (14)
$$

Point symmetric Gauss-Seidel scheme

For the point SGS scheme, terms with coefficients $C_2, \cdots, C_5$ in the left-hand side of Eq. (13) are moved to the right-hand side, and hence only the inversion of C_1 becomes necessary. For time advancement, the computation is carried out in forward and backward sweeps. For a forward sweep, the calculation domain is swept from lower left to upper right via

$$C_1 \overline{\Delta Q_{i,j}^n} = -R_{i,j}^n - C_2 \overline{\Delta Q_{i-1,j}^n} - C_3 \overline{\Delta Q_{i,j-1}^n} - C_4 \widetilde{\Delta Q_{i+1,j}^n} - C_5 \widetilde{\Delta Q_{i,j+1}^n} \quad (15)$$

For a backward sweep, the calculation domain is swept from upper right to lower left.

$$C_1 \Delta Q_{i,j}^n = -R_{i,j}^n - C_2 \widetilde{\Delta Q_{i-1,j}^n} - C_3 \widetilde{\Delta Q_{i,j-1}^n} - C_4 \Delta Q_{i+1,j}^n - C_5 \Delta Q_{i,j+1}^n \quad (16)$$

In the above, $\overline{\Delta Q}$ represents the intermediate solution updated as the forward sweep proceeds, $\widetilde{\Delta Q}$ is the solution available which is not yet updated. $\widetilde{\Delta Q}$ is normally taken to be zero at the first cycle. ΔQ is the solution from the backward sweep. The forward and backward sweep processes can be repeated to better update ΔQ with $\widetilde{\Delta Q}$ computed from previous sweep. Note that the coefficient matrices, $C_1, \cdots, C_5$, remain unchanged during the sweep. As we shall see multiple sweeps with fixed Δt can improve convergence property.

Line symmetric Gauss-Seidel scheme

Equation (13) can be solved using the line SGS scheme with the same coefficient matrices for the point SGS scheme. The domain is swept in forward and backward along one coordinate direction. A block tridiagonal matrix equation is solved at each line perpendicular to the sweep direction. If the ξ direction is chosen as a sweep direction, the forward and backward sweep processes can be written as

$$C_3 \overline{\Delta Q_{i,j-1}^n} + C_1 \overline{\Delta Q_{i,j}^n} + C_5 \overline{\Delta Q_{i,j+1}^n} = - R_{i,j}^n - C_2 \overline{\Delta Q_{i-1,j}^n} - C_4 \widetilde{\Delta Q_{i+1,j}^n} \qquad (17)$$

$$C_3 \Delta Q_{i,j-1}^n + C_1 \Delta Q_{i,j}^n + C_5 \Delta Q_{i,j+1}^n = - R_{i,j}^n - C_2 \overline{\Delta Q_{i-1,j}^n} - C_4 \Delta Q_{i+1,j}^n \qquad (18)$$

Lower-Upper symmetric Gauss-Seidel scheme

The LU-SGS scheme [2] approximates as follows the split Jacobian matrices of inviscid fluxes to guarantee diagonal dominance.

$$\widehat{A}^{\pm} = \frac{1}{2}\left[\widehat{A} \pm \beta_f \, r(\widehat{A}) I \right] \qquad (19)$$

$$\widehat{B}^{\pm} = \frac{1}{2}\left[\widehat{B} \pm \beta_f \, r(\widehat{B}) I \right] \qquad (20)$$

where $r(\widehat{A})$ and $r(\widehat{B})$ are the spectral radii of the flux Jacobians $\widehat{A}$ and $\widehat{B}$ corresponding to the ξ and η directions, respectively, and β_f is a relaxation parameter larger than one. The coefficient matrices of Eq. (13) constructed according to these algorithms can be written as

$$
\begin{aligned}
C_1 &= \frac{I}{J\Delta t} + \left[r(\widehat{A}_{i,j}) + r(\widehat{B}_{i,j}) \right] I + \frac{1}{J} Z_{i,j} \\
C_2 &= - \widehat{A}^{+}_{i-1,j} \qquad\qquad C_3 = - \widehat{B}^{+}_{i,j-1} \\
C_4 &= \widehat{A}^{-}_{i+1,j} \qquad\qquad C_5 = \widehat{B}^{-}_{i,j+1}
\end{aligned}
\qquad (21)
$$

With these coefficient matrices, Eq. (13) is solved by the following two sweeps as in the case of point SGS scheme. The forward sweep process is written as

$$C_1 \overline{\Delta Q_{i,j}^n} = - R_{i,j}^n - C_2 \overline{\Delta Q_{i-1,j}^n} - C_3 \overline{\Delta Q_{i,j-1}^n} - C_4 \widetilde{\Delta Q_{i+1,j}^n} - C_5 \widetilde{\Delta Q_{i,j+1}^n} \qquad (22)$$

and the backward sweep process is written as

$$C_1 \Delta Q_{i,j}^n = - R_{i,j}^n - C_2 \overline{\Delta Q_{i-1,j}^n} - C_3 \overline{\Delta Q_{i,j-1}^n} - C_4 \Delta Q_{i+1,j}^n - C_5 \Delta Q_{i,j+1}^n \qquad (23)$$

In Eq. (20), the coefficient C_1 is a block matrix because of the presence of thermochemical source Jacobian Z. Thus the inversion of block matrix C_1 is required in the forward and backward sweep processes.

Results and Discussions

The algorithms discussed above were applied to solve the flowfields of two cases of hypersonic nonequilibrium flows over blunt body. The first case is the flow over 2D cylinder experimentally studied by Hornung [12] and the second case is the flow over hemisphere at conditions corresponding to the peak heating condition during reentry flight of an SSTO vehicle [13]. The performances of three implicit schemes, point SGS, line SGS, and LU-SGS, against these two flow cases were compared.

Hornumg's Experiment

Hornung [12] studied experimentally a partially dissociated nitrogen gas flow around a two-dimensional cylinder with a radius of $2.54cm$. The freestream conditions of the experiment are:

$$V_\infty = 5.59 \ km/s \ , \ \rho_\infty = 5.349 \times 10^{-3} \ kg/m^3 \ . \ T_\infty = 1833 \ ^\circ K \ , \ T_{v_\infty} = 1833 \ ^\circ K \ , \ c_{N2} = 0.927 \ , \ c_N = 0.073$$

The freestream Mach number is 6.13 and the Reynolds number based on the body radius is 12000. In the present computation, the wall was assumed to be noncatalytic and its temperature was set to 1833 $^\circ K$. The computational domain included half of the body, and calculations were performed on three grid resolutions : 20×40 , 30×60 , and 40×80 grid points in the direction along the surface and normal to the surface, respectively. We used fixed time step with the maximum CFL number of 30 for all computations. In order to avoid computational instability caused by a sudden variation of flow variables during the initial phase of computation, the CFL number was increased from the initial value of 0.1 to the final value of 30 by using a cubic polynomial function of the fractional iteration number, i/N . N is the iteration number at which the final value is attained and i is the current iteration number. For the point SGS and line SGS scheme, N was set to 300. The LU-SGS scheme required slower increment of the CFL number than the point SGS and the line SGS scheme for stable computation. For this case, N was set to 500.

Figures 1, 2, and 3 show respectively the plots of convergence histories of L_2 norm of density residual versus CPU seconds on a DIGITAL workstation 433a for the 20×40 , 30×60 and 40×80 grid system. The number on the line of the plot designates the number of forward and backward sweep cycles. Comparison of the plots points out that the line SGS scheme takes least CPU time for converged solution and the LU-SGS scheme longest CPU time for all the grid systems. The point SGS scheme requires slightly longer CPU time than the line SGS scheme. Convergence is considerably improved by the multiple sweeps for both the point SGS and the LU-SGS scheme. For the point SGS scheme (Figures 1(a), 2(a), and 3(a)), the convergence becomes faster up to three sweep cycles but becomes slightly slower for the case of four sweep cycles. For the LU-SGS scheme (Figures 1(c), 2(c), and 3(c)), the convergence becomes faster as the number of sweep cycles increases. For both schemes, the rate of improvement is
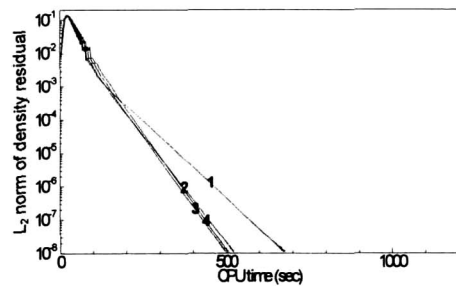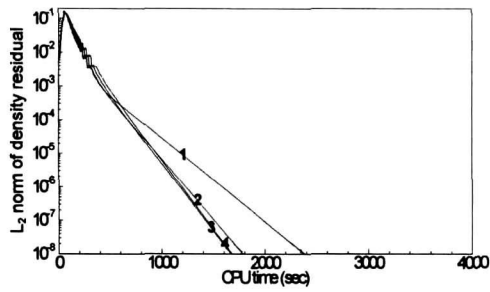

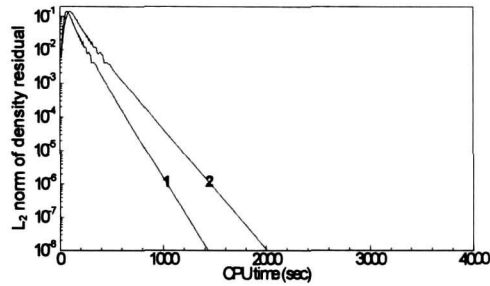(a) point SGS scheme
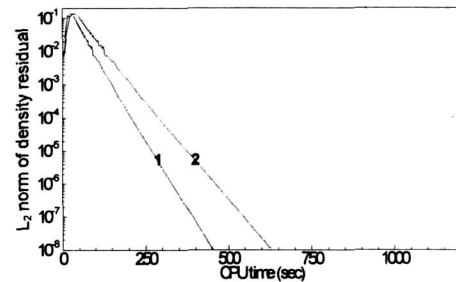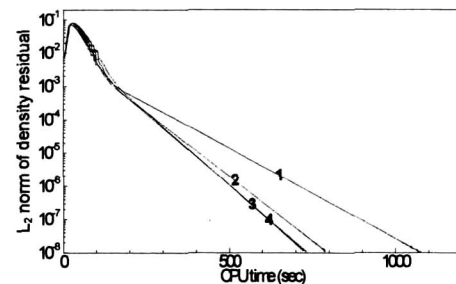
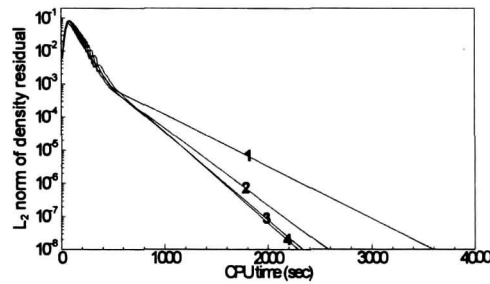(b) line SGS scheme

(c) LU-SGS scheme

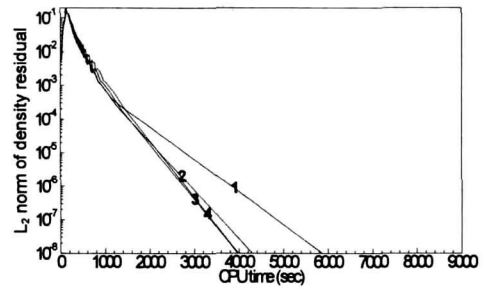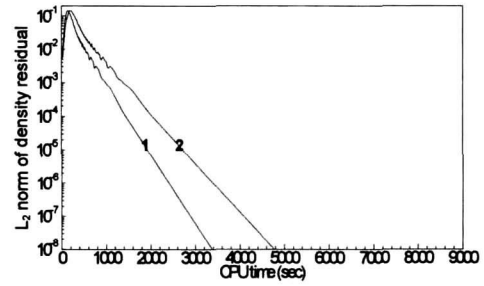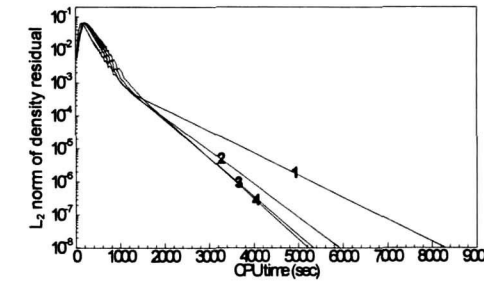**Fig. 1. Convergence history for the flow over 2D cylinder (20×40 grid)**

Chang Ho Lee and Seung O Park

(a) point SGS scheme

(a) point SGS scheme

(b) line SGS scheme

(b) line SGS scheme

(c) LU–SGS scheme

(c)LU–SGS scheme

Fig. 2. Convergence history for the flow over 2D cylinder (30×60 grid)

Fig. 3. Convergence history for the flow over 2D cylinder (40×80 grid)

seen to be largest when two sweep cycles are taken. On the contrary, for the line SGS scheme, the convergence becomes slower when we adopt more than one sweep cycle as illustrated in Figures 1(b), 2(b) and 3(b). From these results, we see that multiple sweep cycles for the point SGS and LU-SGS schemes help the propagation of updated solutions in the computational domain.

In Figure 4, computed pressure and translational temperature distributions along the stagnation grid comparison with the experimental one of Hornung. The present result is seen to be in agreement with the experimental data in both shock shape and fringe patterns. Computations with the point SGS, the line SGS, and the LU-SGS schemes yielded the same computational data.streamline are illustrated for three grid resolutions. The solutions at the shock become more refined as the grid is refined. Figure 5 depicts the numerical interferogram constructed from the density and mass fraction of atomic nitrogen for the 30×60 grid comparison with the experimental one of Hornung. The present result is seen to be in good agreement with the experimental data in both shock shape and fringe patterns. Computations with the point SGS, the line SGS, and the LU-SGS schemes yielded the same computational data.
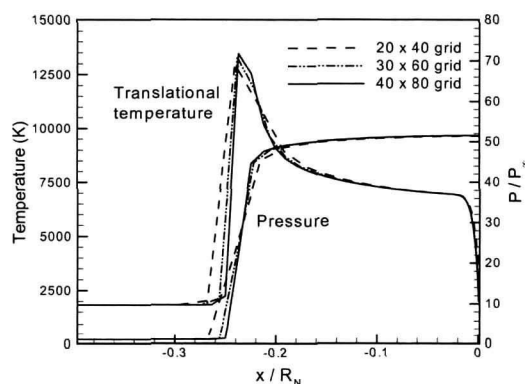
Fig. 4. Pressure and traslational temperature profile along the stagnation streamline

**Fig. 5.** Comparison of interfegrams from experiment [11] and computation

SSTO Reentry Condition

The second case is an axisymmetric flow over a hemisphere with nose radius $R_N = 1.38\,m$ at an altitude of $65\,km$. The freestream conditions are:

$$V_\infty = 5700\ m/s\ ,\ \rho_\infty = 1.641 \times 10^{-4}\ kg/m^3\ .\ T_\infty = 233\ ^\circ K\ ,\ T_{v_\infty} = 233\ ^\circ K\ ,\ c_{N2} = 0.7381\ ,\ c_{O2} = 0.2619$$

The freestream Mach number is 18.6 and the Reynolds number based on the body radius is 85500 . This condition corresponds to the peak heating condition of SSTO reentry [13]. The wall was assumed to be noncatalytic and the temperature was fixed at 1000 $^\circ K$. Calculations were performed again on a 30×60 grid. The flow in this case has thinner boundary layer and thinner shock layer than the first case due to high Mach number, high Reynolds number, and axisymmetric geometry. The grid system near the wall was therefore highly clustered in the normal direction to resolve the boundary layer. We used the maximum CFL number of 10 for this case. The CFL number was increased from the initial value of 0.1 to the final value of 10 in the same manner as was done for the first case. However, the LU-SGS scheme required much lower value of CFL number for stable calculation in the initial phase of iteration. Many attempts were made to get the converged solution. Among those trials, the following way of setting up CFL number yielded the converged solution. The CFL number was increased from 0.1 to 2 with $N = 100$. Then the CFL number of 2 was used up to the 1000*th* iteration. After the 1000*th* iteration, the CFL number was increased from 2 to 10 with $N = 1500$.

Figures 6(a), 6(b), and 6(c) show the convergence histories of the point SGS, the line SGS, and the LU-SGS scheme respectively. The point SGS scheme takes least CPU time and the LU-SGS scheme longest CPU time. The line SGS scheme turns out to be slightly slower than the point SGS scheme for this case. For the point SGS scheme, the convergence is faster with two sweep cycles than three sweep cycles (Figure 6(a)). For the LU-SGS scheme, both two and three sweep cycles result in similar convergence history (Figure 6(c)). As for the first case, multiple sweeps do not improve the convergence for the line SGS scheme (Figure 6(b)). Mass fraction distributions of the five species along the stagnation streamline are shown in Figure 7. We see that in the shock layer, the dissociation of oxygen molecules is almost complete while the dissociation of nitrogen molecules is incomplete. In Figure 8, the profiles of translational and vibrational temperatures along the stagnation streamline are presented. The
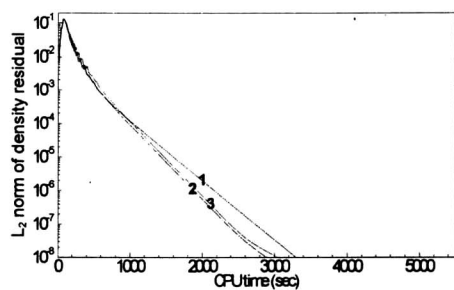
(a) point SGS scheme
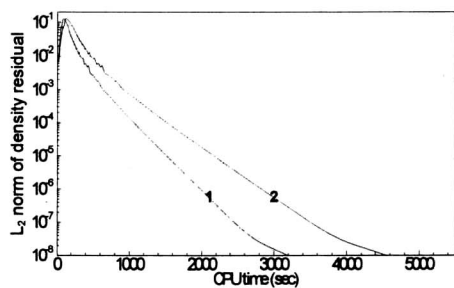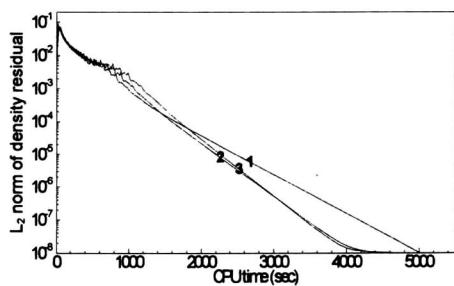
(b) line SGS scheme

(c)LU-SGS scheme

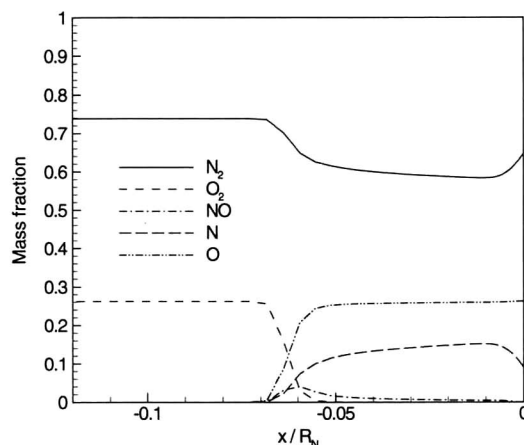Fig. 6. Convergence history for the flow over a sphere

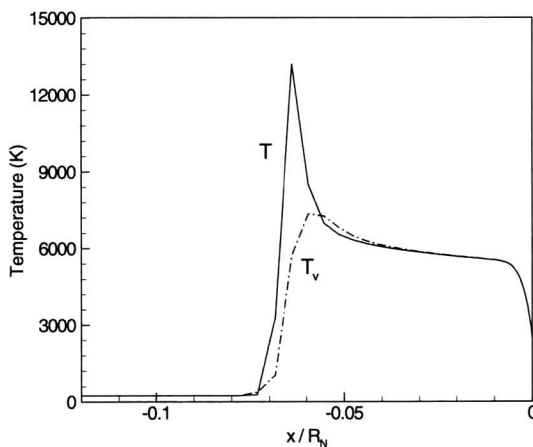Fig. 7. Species mass fractions along the stagnation streamline

Fig. 8. Temperature profiles along the stagnation streamline

translational temperature increases very rapidly to a peak of about $13000K$ past the shock. The vibrational temperature also increases rapidly, but slow than the translational temperature past shock and equilibrates with the translational temperature afterwards.

Conclusions

To compare the performances of implicit schemes, point SGS, line SGS, and LU-SGS schemes, numerical simulations were carried out for nonequilibrium hypersonic flows: the dissociated nitrogen gas flow over 2D cylinder and the air flow over hemisphere at an SSTO reentry condition. Comparison of the convergence histories with respect to CPU time indicated that the point SGS scheme with multiple forward and backward sweeps was as robust and efficient as the line SGS scheme. For the point SGS and the LU-SGS scheme, multiple sweep strategy was found to improve the convergence. The rate of improvement was largest with

two sweep cycles for both schemes. On the contrary, for the line SGS scheme, multiple sweeps deteriorated the convergence property.

References

1. Candler, G.V., and MacCormack, R.W., "Computation of Weakly Ionized Hypersonic Flows in Thermochemical Nonequilibrium," Journal of Thermophysics and Heat Transfer, Vol. 5, No. 3, 1991, pp. 266-273.

2. Park, C., and Yoon, S., "Fully Coupled Implicit Method for Thermochemical Nonequilibrium Air at Suborbital Flight Speeds," Journal of Spacecraft and Rockets, Vol. 28, No. 1, 1991, pp. 31-39.

3. Eberhardt, S., and Imlay, S., "Diagonal Implicit Scheme for Computing Flows with Finite Rate Chemistry," Journal of Thermophysics and Heat Transfer, Vol. 6, No. 2, 1992, pp. 208-216.

4. Hassan, B., Candler, G.V., and Olynick, D.R., "Thermochemical Nonequilibrium Effects on the Aerothermodynamics of Aerbraking Vehicles," Journal of Spacecraft and Rockets, Vol. 30, No. 6, 1993, pp. 647-655.

5. Edwards, J.R., "An Implicit Multigrid Algorithm for Computing Hypersonic, Chemically Reacting Viscous Flows," Journal of Computational Physics, Vol. 123, 1996, pp. 84-95.

6. Ok, H., Development of an Incompressible Navier-Stokes Solver and Its Application to the Calculation of Separated Flows, Ph. D. Thesis, University of Washington. 1993.

7. Schroder, W., and Hartman, G., "Implicit Solutions of Three-Dimensional Viscous Hypersonic Flows," Computers and Fluids, Vol. 21, No. 1, 1992, pp. 109-132.

8. Park, C., Nonequilibrium Hypersonic Aerothermodynamics, Wiley, New York, 1990.

9. Park, C., "Review of Chemical-Kinetic Problems of Future NASA Missions, I: Earth Entries," Journal of Thermophysics and Heat Transfer, Vol. 7, No. 3, 1993, pp. 385-39.

10. Lee, C.H., and Park, S.O., "Computations of Hypersonic Flows over Blunt Body Using a Modified Low-Diffusion Flux-Splitting Scheme," Computational Fluid Dynamics Journal, To appear, 2001.

11. Anderson, W.K., Thomas, J.L., and van Leer, B., "Comparison of Finite Volume Flux Vector Splittings for the Euler Equations," AIAA Journal, Vol. 24, No. 9, 1986, pp. 1453-1460.

12. Hornung, H.G., "Nonequilibrium Dissociating Nitrogen Flow over Spheres and Cylinders," Journal of Fluid Mechanics, Vol. 53, Pt. 1, 1972, pp. 149-176.

13. Gupta, R.N., and Lee, K.P., "Thermo-Chemical Nonequilibrium Analysis of Viscous Shock Layers," AIAA Paper 95-2083, 1995.